International Journal of Nanomedicine

Dovepress
Taylor & Francis Group

Open Access Full Text Article

ORIGINAL RESEARCH

An Active-Targeted ZIF8-Based Nanotheranostic Platform for Ultrasound Imaging-Guided Synergistic Therapy of Triple-Negative Breast Cancer

Xiaoxiao Li[1], Qi Zhou[2], Shaobo Duan[3], Linlin Zhang[2], Zesheng Li[2], Si Chen[2], Yue Yuan[2], Yuanyuan Liu[2], Yanghui Li[2], Xiguo Cai[4], Yuzhou Wang[5], Lianzhong Zhang[1,3,4]

[1]Department of Ultrasound, Henan University People's Hospital, Henan Provincial People's Hospital, Zhengzhou, 450003, People's Republic of China; [2]Department of Ultrasound, Zhengzhou University People's Hospital, Henan Provincial People's Hospital, Zhengzhou, 450003, People's Republic of China; [3]Department of Ultrasound, Henan Provincial International Joint Laboratory of Ultrasonic Nanotechnology and Artificial Intelligence in Precision Theragnostic Systems, Zhengzhou, 450003, People's Republic of China; [4]Henan Provincial Clinical Research Center for Rehabilitation Medicine, Zhengzhou, 450003, People's Republic of China; [5]College of Materials Engineering, Henan University of Engineering, Zhengzhou, 450000, People's Republic of China

Correspondence: Lianzhong Zhang, Department of Ultrasound, Henan University People's Hospital, Henan Provincial People's Hospital, Zhengzhou, 450003, People's Republic of China, Email zlz8777@163.com; Yuzhou Wang, College of Materials Engineering, Henan University of Engineering, Zhengzhou, 450000, People's Republic of China, Email wangyuzhoumse@163.com

Purpose: To address the therapeutic challenges associated with triple-negative breast cancer (TNBC), we developed a folic acid-polyethylene glycol-modified ZIF8-based nanotheranostic platform (FA-PEG@ZIF8@CIP) designed to integrate synergistic sonodynamic therapy, chemotherapy, and immune activation for enhanced antitumor treatment.

Methods: FA-PEG@ZIF8@CIP was constructed as a folic acid-polyethylene glycol-functionalized ZIF8 nanoplatform for the delivery of ciprofloxacin. In this system, ciprofloxacin acted as both a sonosensitizer and a chemotherapeutic agent, while the ZIF8 carrier provided pH-responsive release behavior in the acidic tumor microenvironment. The platform was further evaluated for its physicochemical properties, cellular uptake, antitumor efficacy, immune activation, and ultrasound imaging performance through a series of in vitro and in vivo experiments.

Results: FA-PEG@ZIF8@CIP exhibited favorable tumor-targeting capability and potent antitumor activity. Under ultrasound irradiation, the platform markedly enhanced reactive oxygen species (ROS) generation, leading to effective tumor cell killing. In addition, it induced immunogenic cell death (ICD), as evidenced by enhanced calreticulin exposure, HMGB1 translocation, and extracellular ATP release. These effects further promoted dendritic cell maturation and increased cytotoxic T-lymphocyte infiltration within tumor tissues, indicating activation of antitumor immune responses. The proportions of $CD8^+$ T cells in tumor tissues and spleen increased to 18.7% and 14.6%, respectively, corresponding to approximately 3.0-fold and 2.9-fold increases over the PBS group. The antitumor efficacy of FA-PEG@ZIF8@CIP+US was 4.21-fold higher than that of PBS. Moreover, the platform demonstrated effective ultrasound imaging capability, supporting its application for imaging-guided therapy. Collectively, these findings suggest that FA-PEG@ZIF8@CIP exerts therapeutic effects through the coordinated actions of sonodynamic therapy, chemotherapy, and immune modulation.

Conclusion: This multifunctional nanosystem enables the integration of diagnosis and therapy and represents a promising strategy for TNBC treatment. By combining targeted delivery, pH-responsive drug release, ultrasound imaging, and synergistic therapeutic effects within a single platform, FA-PEG@ZIF8@CIP may offer a valuable approach for improving theranostic outcomes in TNBC.

Keywords: metal-organic frameworks, folic acid response, immunogenic cell death, sonodynamic therapy, breast cancer theranostics

https://doi.org/10.2147/IJN.S589815
Received: 8 January 2026
Accepted: 1 April 2026
Published: 12 April 2026

Introduction

Breast cancer (BC) remains one of the most common and lethal malignancies among women worldwide.[1] Among its molecular subtypes, triple-negative breast cancer (TNBC) is particularly aggressive and is associated with poor prognosis because of the lack of effective therapeutic targets.[2–4] These limitations significantly restrict current treatment options and underscore the urgent need for more effective therapeutic strategies.

Sonodynamic therapy (SDT) has recently attracted increasing attention as a non-invasive anticancer modality because of its deep tissue penetration, high spatial controllability, and favorable biosafety profile.[5] Under ultrasound irradiation, sonosensitizers accumulated in tumor tissues can generate reactive oxygen species (ROS), leading to direct tumor cell destruction.[6,7] In addition, SDT can induce immunogenic cell death (ICD), thereby triggering antitumor immune responses.[8] These features make SDT a promising strategy for breast cancer treatment. However, its therapeutic efficacy is still limited by the intrinsic shortcomings of conventional sonosensitizers, including poor bioavailability, insufficient tumor targeting, inadequate ROS generation, and unsatisfactory stability.[9] Therefore, the development of safe and efficient sonosensitizing platforms is essential for improving SDT efficacy and facilitating its translational application in oncology.[10,11] In parallel, sustained ROS generation by AIE-based organic nanomedicines has been shown to enhance ICD, repolarize macrophages, and activate durable antitumor immunity, highlighting the value of coupling oxidative stress with immune remodeling in cancer therapy.[12]

Recent advances in nanotechnology have greatly expanded the potential of SDT.[11] Among various nanomaterials, metal-organic frameworks (MOFs) have emerged as versatile platforms for biomedical applications. In particular, zeolitic imidazolate framework-8 (ZIF-8), a representative MOF, has attracted considerable interest because of its tunable pore structure, high specific surface area, and good loading capacity for therapeutic agents and biomolecules.[13–19] In addition, ZIF-8 exhibits pH-responsive degradation under weakly acidic conditions, allowing controlled drug release within the tumor microenvironment.[13,14,20] This feature is especially relevant because the aberrant metabolism and rapid proliferation of tumor cells are typically accompanied by extracellular acidification. Beyond its function as a carrier, the degradation of ZIF-8 releases Zn^{2+}, which has been reported to exert antitumor effects. More importantly, recent studies have suggested that ZIF-8 may also participate directly in SDT: unsaturated Zn–N sites on its surface can facilitate electron transfer under ultrasound stimulation, promoting ROS generation, while its cavitation-related behavior may further enhance sonodynamic performance.[7,21,22] Owing to these properties, ZIF-8 represents a promising multifunctional platform for imaging-guided cancer therapy. This imaging-guided concept is also clinically relevant because recent machine-learning analysis has suggested that incorporating breast sonography can improve the prediction of pathological complete response after neoadjuvant therapy in breast cancer.[23]

To further improve therapeutic efficacy, we introduced ciprofloxacin (CIP) into the ZIF-8 system. CIP is a fluoroquinolone antibiotic with favorable bioavailability and safety, and accumulating evidence suggests that it can be repurposed for anticancer applications.[24,25] Previous studies have shown that CIP inhibits topoisomerase II, thereby suppressing tumor cell proliferation, migration, and metastasis, and it has also been reported to possess sonosensitizing activity.[26,27] In the present study, CIP was incorporated into ZIF-8 through physical adsorption, electrostatic interactions, and coordination, enabling combined chemo-sonodynamic effects.[28] Upon exposure to the acidic tumor microenvironment, ZIF-8 degrades and releases both CIP and Zn^{2+}. CIP contributes directly to tumor cell killing and can enhance ROS accumulation during SDT, whereas released Zn^{2+} may further strengthen the antitumor effect.[21,27,29,30] In addition, CIP has been associated with ICD-related immune activation, suggesting its potential to amplify antitumor immunity when combined with SDT.[31,32]

Despite these advantages, the tumor-targeting efficiency of ZIF-8 and CIP remains limited, which may reduce intratumoral drug accumulation and compromise treatment efficacy. To address this issue, we further functionalized ZIF8@CIP with folic acid-polyethylene glycol (FA-PEG). Folic acid is a widely used targeting ligand because folate receptor α (FRα) is overexpressed in a variety of tumor cells, allowing receptor-mediated endocytosis and selective intracellular delivery.[33–36] Surface modification with FA-PEG can therefore improve the stability, biocompatibility, and tumor-targeting capability of the nanoplatform.[37,38] Similarly, recent biomimetic work has shown that improved tumor targeting and prolonged circulation can substantially enhance therapeutic efficacy against breast cancer metastasis and

rechallenge.[39] After cellular internalization, the acidic intracellular environment promotes ZIF-8 degradation and controlled CIP release, thereby improving therapeutic selectivity and efficacy.[40]

Based on this rationale, we developed an FA-PEG-functionalized, CIP-loaded ZIF-8 nanoplatform for TNBC treatment. This system was designed to integrate targeted delivery, pH-responsive drug release, sonodynamic therapy, chemotherapy, immune activation, and ultrasound imaging into a single platform. By combining these functions, the proposed nanoplatform aims to overcome the limitations of conventional monotherapies and provide an effective theranostic strategy for TNBC.

Materials and Methods

Materials

Xi'an Tianmao Chemical Co., Ltd. 2-Methylimidazole was provided by Shanghai Macklin Biochemical Co., Ltd. CIP was obtained from APEXBIO (USA). FA-PEG was sourced from Shanghai Yuanye Biotechnology Co., Ltd. ATP assay kit, Hoechst 33342, 2',7'-dichlorofluorescin diacetate (DCFH-DA), Calcein-AM, and propidium iodide (PI) were all purchased from Beijing Solarbio Science & Technology Co., Ltd. The Cell Counting Kit-8 (CCK-8) for cell proliferation and cytotoxicity assay kit was acquired from Dongren Chemical Technology Co., Ltd.

Cells and Animals

The 4T1 cell and the MDA-MB-231 lines were obtained from the National Experimental Cell Resource Sharing Platform (Beijing, China). All cell lines were maintained in DMEM supplemented with 10% fetal bovine serum (FBS) and 1% penicillin-streptomycin at 37°C in a humidified atmosphere containing 5% CO_2. Healthy 6-8-week-old BALB/c mice were purchased from the Experimental Animal Center of Zhengzhou University. The animals were housed under controlled conditions at 17–25°C, 45–80% humidity, with a 12-hour light/dark cycle. For humane euthanasia of the experimental BALB/c mice, the cervical dislocation method was performed by well-trained individuals. The specific operation was as follows: the operator placed the thumb and index finger on either side of the mouse's neck at the base of the skull, then grasped the base of the tail with the other hand and pulled quickly to separate the cervical vertebrae from the skull. Death was confirmed by the absence of corneal reflex and spontaneous respiration. All experimental procedures were approved by the Institutional Animal Care and Use Committee of Zhengzhou University (Approval No. ZZU-LAC20241227[07]). All the animal experiments were conducted in accordance with the American Veterinary Medical Association.

Synthesis of FA-PEG@ZIF8@CIP

Preparation of ZIF8

ZIF-8 nanoparticles were prepared by a simple aqueous self-assembly method. Briefly, 2-methylimidazole (2-MIM, 28 g) and zinc acetate dihydrate (6 g) were separately dissolved in 100 g of deionized water. Subsequently, 5.12 g of the 2-MIM solution was placed in a glass vial, and 5.3 g of the zinc acetate dihydrate solution was added dropwise at a constant rate to minimize excessive disturbance during mixing. The mixture was gently stirred with a glass rod for approximately 30s, after which a milky white suspension was formed, indicating the generation of ZIF-8 nanoparticles. The reaction mixture was then sealed and allowed to stand at room temperature for 2 h. After incubation, the precipitate was collected by centrifugation at 9,000 rpm for 15 min and washed once with deionized water, followed by centrifugation at 9,000 rpm for 10 min. The obtained pellet was finally redispersed in deionized water and dried overnight in an oven at 105 °C.

Preparation of ZIF8@CIP

To prepare ZIF-8@CIP, 100 mg of activated ZIF-8 was dispersed in 10 mL of an aqueous ciprofloxacin solution (10 mg/mL). The mixture was magnetically stirred under sealed conditions at room temperature for 48 h to allow sufficient drug loading. After incubation, the resulting ZIF-8@CIP composite was collected and washed three times with methanol by filtration to remove unbound ciprofloxacin. The final product was then dried under vacuum at 60 °C for 12 h to obtain a white powdered solid.

Preparation of FA-PEG@ZIF8@CIP

FA-PEG@ZIF-8@CIP was prepared by surface modification of ZIF-8@CIP with FA-PEG. Briefly, 25 mg of FA-PEG was dissolved in 5 mL of deionized water, followed by the addition of 50 mg of ZIF-8@CIP. The mixture was continuously stirred at room temperature for 48 h under light-protected conditions. After the reaction was completed, the precipitate was collected by centrifugation at 11,000 rpm and washed three times with deionized water to remove unbound FA-PEG. The final product was dried under vacuum to obtain the FA-PEG-modified ZIF-8@CIP composite.

Characterization of Nanoparticles

The morphology and microstructure of the synthesized nanoparticles were characterized by transmission electron microscopy (TEM, JEM-2100, JEOL, Japan) and scanning electron microscopy (SEM, Sigma 300, ZEISS, Germany). The hydrodynamic diameter and zeta potential of ZIF-8, ZIF-8@CIP, and FA-PEG@ZIF-8@CIP were determined using a Mastersizer 3000 instrument, and all measurements were performed in triplicate. The crystal structures of the nanoparticles were analyzed by X-ray diffraction (XRD) using a D8 Advance diffractometer. Ultraviolet-visible (UV-Vis) absorption spectra were recorded with a UV-2550 spectrophotometer to evaluate the optical properties and confirm drug loading. Fourier transform infrared (FTIR) spectra were collected using a Nicolet 6700 spectrometer to identify the characteristic functional groups and verify the successful incorporation of CIP and FA-PEG.

Drug Loading Capacity Determination

The drug loading efficiency (DLE%) of CIP and the entrapment efficiency (EE%) of FA-PEG was measured by UV spectrophotometer at 278 nm and 280nm absorption wavelength, respectively. The solution was established in the concentration range of 5–10 μg/mL. The DLE% and EE% were calculated using the following equations:

$$\mathrm{DLE\%} = \frac{\text{Mass of encapsulated CIP in FA} - \text{PEG@ZIF8@CIP}}{\text{Total mass of FA} - \text{PEG@ZIF8@CIP}} \times 100\%$$

$$\mathrm{EE\%} = \frac{\text{Mass of FA} - \text{PEG in FA} - \text{PEG@ZIF8@CIP}}{\text{Total mass of FA} - \text{PEG}} \times 100\%$$

Hemolysis Assay

The hemocompatibility of FA-PEG@ZIF-8@CIP was evaluated by a hemolysis assay. Briefly, FA-PEG@ZIF-8@CIP dispersions at different concentrations (0, 50, 100, 150, and 200 μg/mL) were incubated with a 2% suspension of freshly collected erythrocytes under physiological conditions (37 °C) for 2 h. After incubation, the samples were centrifuged and the supernatant was collected. The absorbance at 540 nm was measured using a microplate reader (BioTek, USA) to quantify hemoglobin release.

Tumor Targeting Ability of FA-PEG@ZIF8@CIP

The tumor-targeting ability of FA-PEG-modified nanoparticles was evaluated using 4T1 breast cancer cells. Concisely, 4T1 cells were seeded in 6-well plates at a density of 1×10^5 cells per well and cultured in DMEM supplemented with 10% fetal bovine serum and 1% penicillin–streptomycin at 37 °C.

Because the nanoparticles themselves were non-fluorescent, the lipophilic fluorescent dye DiI (10 μM) was used for labeling. After 24 h of cell attachment, the cells were incubated with three different nanoparticle formulations: (A) DiI-labeled ZIF-8@CIP dispersed in folate-deficient DMEM; (B) DiI-labeled FA-PEG@ZIF-8@CIP dispersed in FA-containing DMEM; (C) DiI-labeled FA-PEG@ZIF-8@CIP dispersed in FA-deficient DMEM. Cells were incubated with the nanoparticles for 45 min, followed by washing three times with PBS to remove unbound nanoparticles. The cells were then fixed with 4% paraformaldehyde, and nuclei were stained with Hoechst dye. Fluorescence images were acquired using an inverted fluorescence microscope (Olympus, Japan). DiI and Hoechst signals were detected using separate filter sets corresponding to their respective excitation and emission wavelengths.

Cellular Uptake of FA-PEG@ZIF8@CIP

The cellular uptake behavior of the nanoparticles was further investigated using indocyanine green (ICG) as a fluorescent probe. Briefly, 4T1 cells were seeded in 6-well plates at a density of 1×10^5 cells per well and cultured for 24 h at 37 °C in DMEM supplemented with 10% fetal bovine serum and 1% penicillin–streptomycin.

Cells were then incubated with different drug formulations containing ICG for 1 h or 4 h under dark conditions. After incubation, the cells were washed twice with PBS and stained with Hoechst 33342 for 30 min. The samples were subsequently observed using an inverted fluorescence microscope (Olympus, Japan) to evaluate intracellular fluorescence distribution.

Cytotoxicity Assay Using CCK-8

The cytotoxicity of different formulations was evaluated using the CCK-8 assay. Concisely, 4T1 cells were seeded in 96-well plates and allowed to adhere overnight. The cells were then treated with PBS, PBS + US, ZIF-8@CIP, ZIF-8@CIP + US, FA-PEG@ZIF-8@CIP, or FA-PEG@ZIF-8@CIP + US at various concentrations.

For ultrasound treatment, cells in the US groups were exposed to ultrasound irradiation (1.0 MHz, 1.5 W/cm^2, 50% duty cycle, 1 min) after 12 h of incubation with the nanoparticles. Following ultrasound exposure, the cells were further incubated for an additional 12 h. Cell viability was then determined using a CCK-8 kit according to the manufacturer's instructions, and the absorbance was measured using a microplate reader.

Live/Dead Cell Staining Assay

A Live/Dead staining assay was performed to visually assess cell viability after different treatments. Collectively, 4T1 cells were seeded in 6-well plates and treated with the corresponding formulations. Cells in the ultrasound groups received ultrasound irradiation (1.0 MHz, 1.5 W/cm^2, 50% duty cycle, 1 min).

After treatment, the cells were incubated for an additional 12 h (for ultrasound groups) or 24 h (for non-ultrasound groups). Subsequently, the cells were collected by centrifugation and washed twice with PBS. The cells were then stained with Calcein AM (1 μL) and propidium iodide (0.5 μL) according to the manufacturer's instructions. Fluorescence images were captured using an inverted fluorescence microscope (Olympus, Japan).

ROS Generation Assay

Intracellular ROS generation was evaluated using the fluorescent probe DCFH-DA. Briefly, 4T1 cells were seeded in 6-well plates and cultured for 18–24 h. The cells were then incubated with PBS, ZIF-8@CIP, or FA-PEG@ZIF-8@CIP for 6 h.

For ultrasound treatment, cells in the designated groups were exposed to ultrasound irradiation (1.0 MHz, 1.5 W/cm^2, 50% duty cycle, 1 min). After ultrasound treatment, the cells were further incubated for 4 h and then stained with DCFH-DA. The intracellular fluorescence signals were observed using an inverted fluorescence microscope (Olympus, Japan).

ICD Expression Detection Experiment

To evaluate immunogenic cell death (ICD), the expression of calreticulin (CRT), high mobility group box 1 (HMGB1), and ATP release was analyzed.4T1 cells were cultured and divided into different treatment groups. Cells in the ultrasound groups were exposed to ultrasound irradiation (1.0 MHz, 1.5 W/cm^2, 50% duty cycle, 1 min) after drug treatment.

For CRT detection, treated cells were fixed with 4% paraformaldehyde for 30 min and incubated with a primary antibody against CRT overnight at 4 °C. After washing with PBS, the cells were incubated with FITC-conjugated secondary antibodies for 1 h. The nuclei were counterstained with Hoechst 33342 for 30 min. Fluorescence images were obtained using an inverted fluorescence microscope, and fluorescence intensity was quantified using ImageJ software.For HMGB1 detection, cells were fixed and permeabilized with 0.5% Triton X-100 for 10 min before incubation with an anti-HMGB1 primary antibody. The subsequent staining procedures were the same as those described for CRT detection. ATP release after different treatments was quantified using an ATP detection kit (Solarbio) according to the manufacturer's protocol.

Ultrasound Imaging Experiments

In Vitro Contrast-Enhanced Ultrasound Imaging

For in vitro contrast-enhanced ultrasound imaging, the samples were divided into five groups: PBS, SonoVue (SV), ZIF-8, ZIF-8@CIP and FA-PEG@ZIF-8@CIP. Each sample was prepared as a suspension at different concentrations. The suspensions were transferred into plastic Pasteur pipettes and immersed in ultrapure water for ultrasound imaging. In vitro ultrasound imaging was performed using a color Doppler ultrasound diagnostic system (GE Logiq E9) in both B-mode and contrast-enhanced mode. The contrast-enhancement performance of each sample was evaluated under different mechanical index (MI) settings (0.10, 0.20, 0.30, 0.40, and 0.50). Regions of interest (ROIs) were selected from the contrast-enhanced images for quantitative analysis of ultrasound signal intensity.

In Vivo Contrast-Enhanced Ultrasound Imaging

For in vivo contrast-enhanced ultrasound imaging, female BALB/c mice were randomly divided into five groups: PBS, SV, ZIF-8, ZIF-8@CIP and FA-PEG@ZIF-8@CIP. The mice were anesthetized by intraperitoneal injection of sodium pentobarbital (10 mg/mL, 20 mL/kg), and the tumor area was depilated before imaging. In vivo ultrasound imaging was carried out using a GE Logiq E9 ultrasound diagnostic system equipped with an L12-5 linear array transducer (5–12 MHz). Consistent with the in vitro setting, a MI ranging from 0.1 to 0.5 was selected for contrast-enhanced imaging of the tumor region. Mice in the PBS, SV, ZIF-8, ZIF-8@CIP and FA-PEG@ZIF-8@CIP groups were intravenously injected via the tail vein with 200 μL of PBS, 200 μL of SV (5 mg/mL), 200 μL of ZIF-8 (0.75 mg/mL), 200 μL of ZIF-8@CIP (0.75 mg/mL) and 200 μL of FA-PEG@ZIF-8@CIP (0.75 mg/mL), respectively. Contrast-enhanced ultrasound images of the tumor regions were then acquired, and ROIs were selected for quantitative analysis of ultrasound signal intensity.

In Vivo Animal Fluorescence Imaging

To evaluate the in vivo biodistribution and tumor-targeting ability of the nanoparticles, tumor-bearing mice were randomly divided into two groups (n = 3 per group). Fluorescence imaging was performed using an IVIS imaging system at predetermined time points following intravenous administration of the formulations. At the end of the experiment, the mice were euthanized, and major organs (heart, liver, spleen, lung, and kidney) as well as tumor tissues were excised for ex vivo fluorescence imaging.

In Vivo Antitumor Activity

A subcutaneous 4T1 tumor model was established in female BALB/c mice. Briefly, 4T1 cells (1×10^6) were injected subcutaneously into the flank of the mice. When the tumor volume reached approximately 100 mm^3 (about 7 days after inoculation), the mice were randomly divided into four groups, with 5 mice in each group (G1: PBS, G2: PBS+US, G3: ZIF8@CIP, G4: ZIF8@CIP+US, G5: FA-PEG@ZIF8@CIP, and G6: FA-PEG@ZIF8@CIP+US).

For the ultrasound (US) groups, ultrasound irradiation (1.0 MHz, 2.5 W/cm^2, 50% duty cycle, 5 min) was applied 6 h after drug administration. Tumor volume and body weight were recorded every two days during the treatment period. Tumor volume was calculated using the following formula:

$$Tumor\ volume = \frac{length \times width^2}{2}$$

At the end of the treatment period, mice were sacrificed, and tumor tissues and major organs (heart, liver, spleen, lung, and kidney) were harvested for histological analysis. Hematoxylin and eosin (H&E) staining, Ki67 immunohistochemical staining, and TUNEL assays were performed to evaluate tumor proliferation and apoptosis. In addition, blood samples were collected via retro-orbital bleeding for biochemical analysis.

In Vivo Antitumor Immune Response Assessment

To evaluate immune responses induced by the treatments, lymph nodes, spleens, and tumor tissues were collected from treated mice and processed into single-cell suspensions by mechanical dissociation and filtration through a 40 μm cell strainer.

The immune cell populations were analyzed using a flow cytometer (BD Accuri C6 Plus). Dendritic cell (DC) maturation in lymph nodes was evaluated by detecting $CD11c^+CD80^+CD86^+$ cells. In tumor tissues, multiple immune cell populations were analyzed, including $CD4^+$ T cells, $CD8^+$ T cells, $CD8^+$Granzyme B^+ cytotoxic T cells, and regulatory T cells (Tregs, defined as $CD4^+Foxp3^+$ cells). Additionally, splenic lymphocytes were stained with antibodies against CD3, CD4, CD8, and IFN-γ to evaluate the infiltration of $CD4^+$ and $CD8^+$ T cells and the expression of IFN-γ.

In Vivo Therapy Effect of the Lung Metastasis Model

To evaluate the therapeutic efficacy of the nanoparticles in a lung metastasis model, a subcutaneous 4T1 tumor model was first established in female BALB/c mice. The mice were randomly assigned to four groups, with 5 mice in each group (G1: PBS, G2: ZIF8@CIP, G3: FA-PEG@ZIF8@CIP, and G4: FA-PEG@ZIF8@CIP+US). For the ultrasound groups, ultrasound irradiation (1.0 MHz, 2.5 W/cm^2, 50% duty cycle, 5 min) was applied 6 h after administration.

After the final treatment, lung metastasis was induced by intravenous injection of 4T1 cells (3×10^5) through the tail vein. On day 22, the mice were euthanized, and lung tissues were collected and photographed to record metastatic nodules. The lungs were then fixed in 4% paraformaldehyde and subjected to hematoxylin and eosin (H&E) staining for histological examination.

In Vivo Biosafety Assessment

To evaluate the in vivo biosafety of the nanoparticles, body weight changes of the mice were monitored throughout the treatment period. At the end of the experiment, major organs (heart, liver, spleen, lung, and kidney) were collected for histological examination using H&E staining.

Additionally, blood samples were collected from the mice for serum biochemical analysis to assess potential systemic toxicity.

Statistical Analysis

Statistical evaluations were carried out employing an unpaired Student's *t*-test or one-way ANOVA. The assessment of significance was performed using GraphPad Prism (10.0). Data are presented as the mean± standard deviation (S.D.) ns: no significance, $*p < 0.05$, $**p < 0.01$, $***p < 0.001$, and $****p < 0.0001$.

Results and Discussion

Synthesis and Characterization of FA-PEG@ZIF8@CIP

Scheme 1 illustrates the synthetic route for the FA-PEG@ZIF-8@CIP nanoplatform and its proposed application in cancer theranostics. Briefly, ZIF-8 was first synthesized through the coordination of 2-methylimidazole with Zn^{2+}. Ciprofloxacin (CIP) was then loaded into the ZIF-8 framework through multiple interactions, including electrostatic attraction, hydrogen bonding, and π–π stacking. Finally, FA-PEG was introduced onto the nanoparticle surface to obtain FA-PEG@ZIF-8@CIP (Figure 1A).

The morphology and microstructure of the nanoparticles were examined by scanning electron microscopy (SEM) and transmission electron microscopy (TEM). As shown in Figure 1B and C, both ZIF-8 and FA-PEG@ZIF-8@CIP exhibited well-defined three-dimensional structures. Compared with the typical rhombic dodecahedral morphology of ZIF-8, FA-PEG@ZIF-8@CIP displayed a less regular shape with relatively blurred edges, suggesting successful surface modification after FA-PEG coating. Additionally, hydrodynamic size analysis revealed that both ZIF-8 and FA-PEG @ZIF-8@CIP exhibited relatively uniform particle size distributions (Figure 1D and E), with polydispersity index (PDI) values of 0.218 and 0.239, respectively, indicating their favorable dispersion stability.

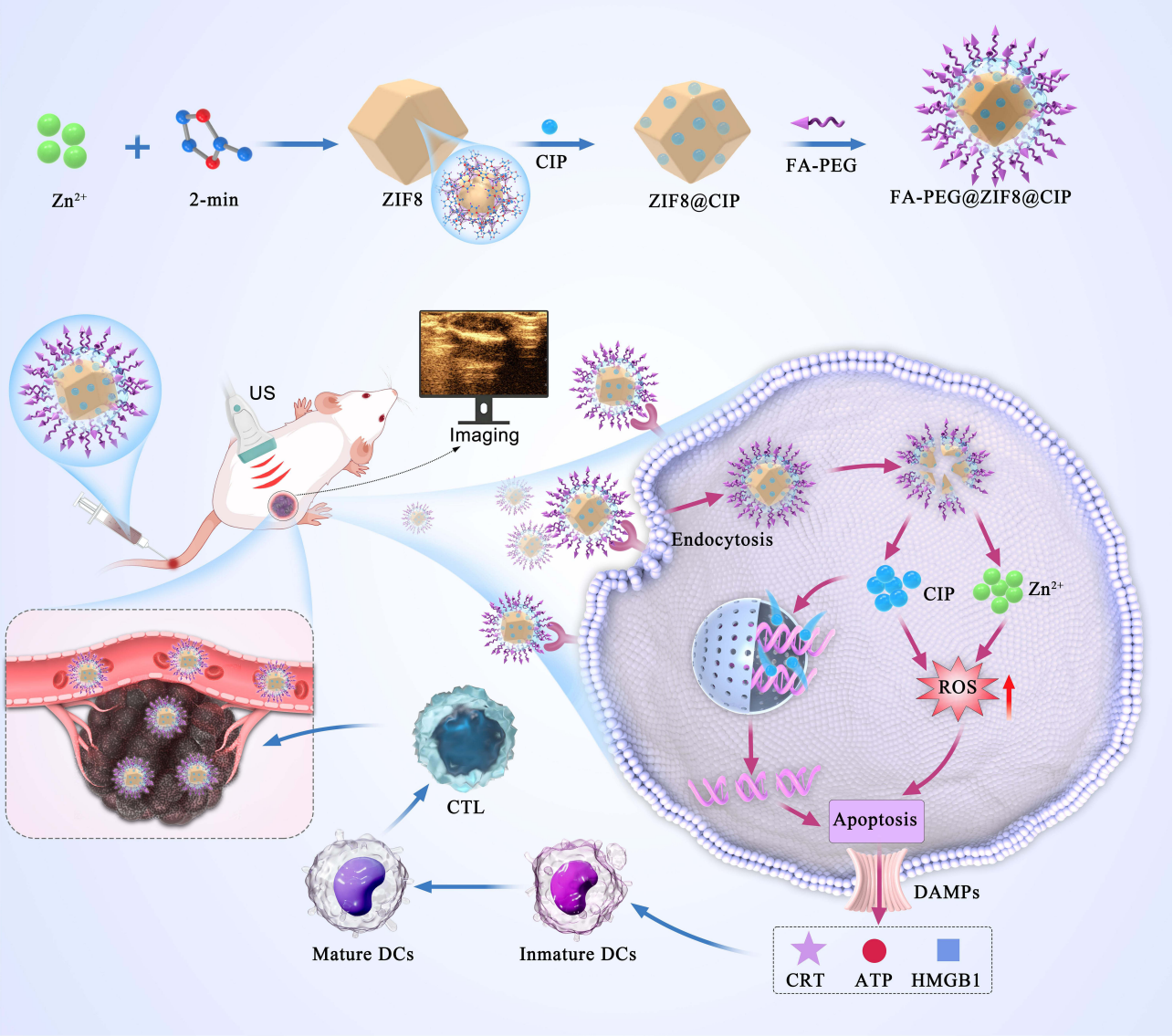

Scheme 1 The synthetic route for the FA-PEG@ZIF-8@CIP nanoplatform and its proposed application in cancer theranostics.

The crystalline structures of ZIF-8, CIP, ZIF-8@CIP, FA-PEG, and FA-PEG@ZIF-8@CIP were further characterized by X-ray diffraction (XRD) (Figure 1F). The diffraction pattern of ZIF-8 was consistent with previously reported data,[41] confirming the successful synthesis of the ZIF-8 framework. Importantly, the characteristic diffraction peaks of ZIF-8 were retained after CIP loading, indicating that the crystalline framework remained intact during the drug-loading process. In addition, the XRD pattern of FA-PEG@ZIF-8@CIP preserved the major diffraction features of ZIF-8, while changes in peak intensity, particularly in the low-angle region, were observed after FA-PEG modification. This finding suggests that surface functionalization with FA-PEG affected the diffraction behavior of the nanoparticles without disrupting the overall ZIF-8 structure.

The surface charge properties of the nanoparticles were assessed by zeta potential measurements. As shown in Figure 1G, the zeta potentials of ZIF-8, ZIF-8@CIP, and FA-PEG@ZIF-8@CIP were +19.24 mV, −15.81 mV, and −10.96 mV, respectively. The positive charge of ZIF-8 is attributable to the presence of Zn^{2+} and imidazole groups on its surface. After CIP loading, the surface potential shifted from positive to negative, which may be associated with the negatively charged carboxyl groups of CIP as well as their interactions with the ZIF-8 framework. Following FA-PEG

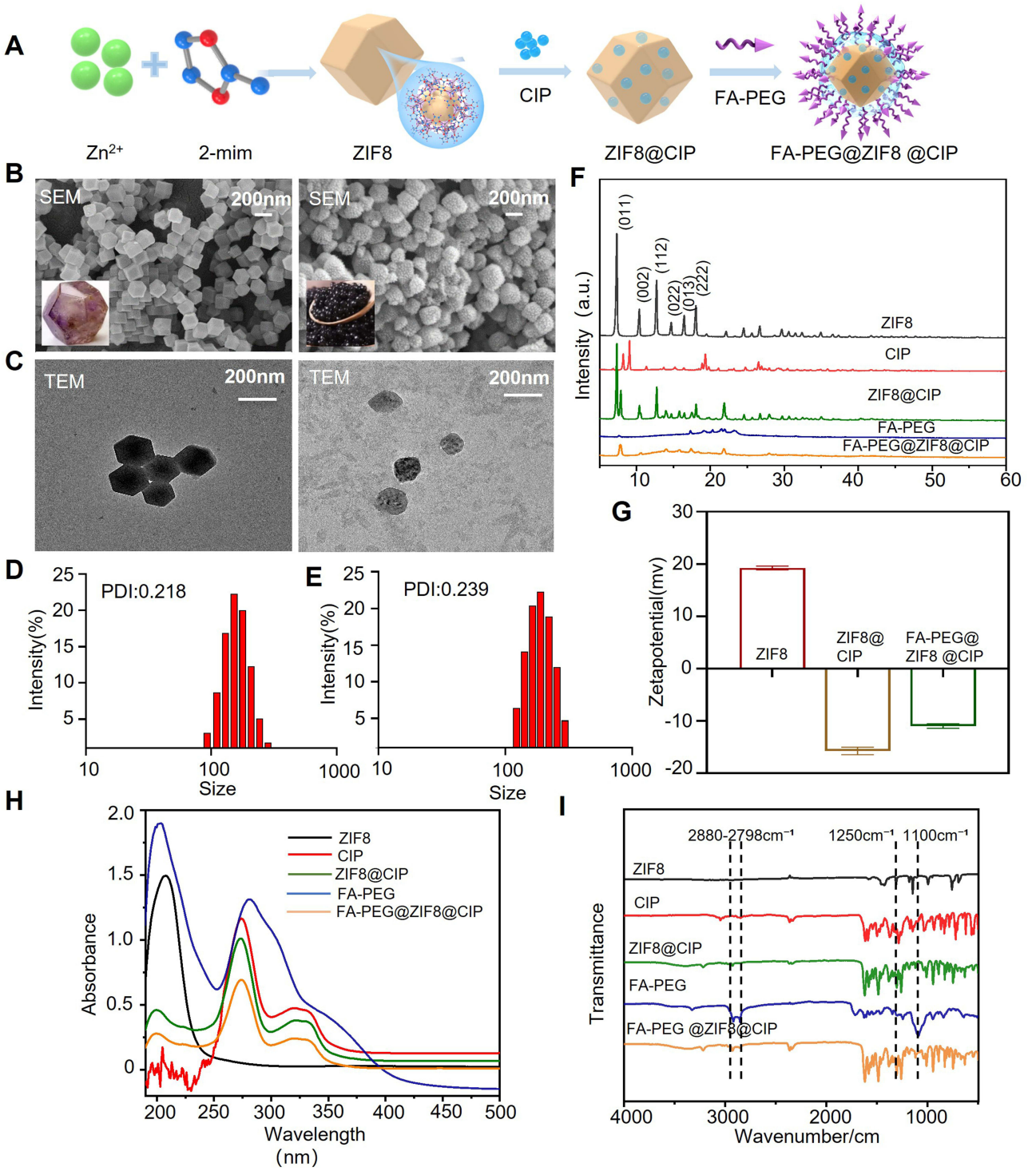

Figure 1 Characterization of FA-PEG@ZIF-8@CIP. (**A**) Schematic illustration of the preparation process of FA-PEG@ZIF-8@CIP. (**B** and **C**) SEM and TEM images of ZIF-8 and FA-PEG@ZIF-8@CIP, respectively. (**D** and **E**) Hydrodynamic size distribution of ZIF-8 and FA-PEG@ZIF-8@CIP, respectively. (**F**) XRD patterns of ZIF-8, CIP, ZIF-8@CIP, FA-PEG, and FA-PEG@ZIF-8@CIP. (**G**) Zeta potentials of ZIF-8, ZIF-8@CIP, and FA-PEG@ZIF-8@CIP. (**H** and **I**) UV–Vis absorption spectra and FT-IR spectra of ZIF-8, CIP, ZIF-8@CIP, FA-PEG, and FA-PEG@ZIF-8@CIP, respectively.

modification, the nanoparticles remained negatively charged, further supporting successful surface functionalization. These stepwise changes in zeta potential are consistent with the sequential loading of CIP and coating with FA-PEG.

UV–Vis spectroscopy further confirmed drug incorporation. As shown in Figure 1H, both ZIF-8@CIP and FA-PEG @ZIF-8@CIP exhibited a characteristic absorption peak at 278 nm, consistent with the absorption profile of CIP,

https://doi.org/10.2147/IJN.S589815

indicating successful encapsulation of CIP in the nanoparticles. Fourier transform infrared (FT-IR) spectra provided additional evidence for nanoparticle assembly and surface modification (Figure 1I). Compared with free CIP, the characteristic peak of CIP at 1250 cm^{-1} showed a red shift after incorporation into the ZIF-8 system, suggesting coordination interactions between the carbonyl groups of CIP and Zn^{2+} within the framework. Moreover, characteristic absorption bands attributed to FA-PEG, including those at 2880–2798 cm^{-1} and 1100 cm^{-1}, were detected in the spectrum of FA-PEG@ZIF-8@CIP, further confirming successful FA-PEG modification.

Based on the standard calibration curve and UV–Vis quantification of CIP and FA-PEG, the DLE of CIP in FA-PEG @ZIF-8@CIP was 57.84% and the EE% of FA-PEG was 50.69%.

Assessment of the in Vitro Antitumor Efficacy of FA-PEG@ZIF8@CIP

As shown in Figure 2A, intracellular red fluorescence was already detectable in the FA-PEG@ZIF-8@CIP group after 1 h of incubation, indicating that the nanoparticles had begun to be internalized by 4T1 cells. After 4 h, the fluorescence intensity was further increased, suggesting enhanced intracellular accumulation over time. To further validate this observation, fluorescence intensity was quantitatively analyzed using ImageJ, and the results are presented in Figure 2B. Quantitative analysis showed that the fluorescence intensity in the FA-PEG@ZIF-8@CIP group was the highest at both 1 h and 4 h among all groups, indicating efficient cellular uptake of FA-PEG@ZIF-8@CIP. In contrast, in MDA-MB-231 cells (which have low folate receptor expression), both the fluorescence signal and the quantified intensity of FA-PEG@ZIF8@CIP remained relatively unchanged between 1 h and 4 h (Figure S1A and B). The markedly lower uptake in these cells, compared to 4T1 cells, confirms that the efficient internalization in high-expressing cells is attributable to the specific binding of FA-PEG to the folate receptor.

We next evaluated the targeting capability of FA-PEG@ZIF-8@CIP. Fluorescence microscopy images of DiI-labeled nanoparticles are shown in Figure S2, in which the nuclei of 4T1 cells were stained with Hoechst (blue) and nanoparticles were labeled with DiI (red). After 50 min of co-incubation, unbound nanoparticles were removed by washing. In the non-targeted ZIF-8@CIP group, only weak red fluorescence was observed around the nuclei (Figure S2**A**), indicating limited cellular association in the absence of FA-mediated targeting. In contrast, cells treated with FA-PEG@ZIF-8@CIP exhibited markedly stronger red fluorescence surrounding the nuclei (Figure S2B and C), suggesting enhanced binding and/or internalization of the nanoparticles. The strongest fluorescence signal was observed in the FA-free DMEM group (Figure S2C), which may be attributed to reduced competition from free folate and more efficient folate receptor-mediated uptake.

Subsequently, the cytotoxicity of different treatments was evaluated by the CCK-8 assay at 100 μg/mL, as shown in Figure 2C. After 24 h of incubation, the PBS group showed negligible cytotoxicity, whereas the PBS + US group exhibited only slight growth inhibition, which may be attributable to the effect of ultrasound alone. In contrast, both ZIF-8@CIP + US and FA-PEG@ZIF-8@CIP + US induced marked cytotoxicity, reducing 4T1 cell viability to 48.0% and 23.3%, respectively, which was significantly lower than that of their corresponding non-ultrasound groups. This enhanced cytotoxicity is likely associated with ultrasound-triggered ROS generation, which promoted tumor cell death. In addition, FA-PEG@ZIF-8@CIP exhibited stronger cytotoxicity than ZIF-8@CIP under the same conditions, suggesting that FA-PEG modification improved cellular uptake and thereby enhanced therapeutic efficacy. We further evaluated the effects of different concentrations of ZIF-8@CIP, ZIF-8@CIP + US, FA-PEG@ZIF-8@CIP, and FA-PEG @ZIF-8@CIP + US on 4T1 cells (Figure S3). The results demonstrated a concentration-dependent inhibitory effect, with increasing concentrations resulting in progressively lower cell viability. Moreover, ultrasound further enhanced the cytotoxic effect of both nanoparticle formulations. Taken together, these findings indicate that FA-PEG@ZIF-8@CIP combined with ultrasound exerts the strongest inhibitory effect on 4T1 cell viability.

These results were further supported by live/dead staining (Figure 2D). Compared with the other groups, the FA-PEG @ZIF-8@CIP + US group showed markedly increased red fluorescence and reduced green fluorescence, indicating extensive cell death after treatment. In contrast, the FA-PEG@ZIF-8@CIP group without ultrasound treatment displayed predominantly green fluorescence, suggesting limited cytotoxicity in the absence of ultrasound activation. These observations further confirm the pronounced in vitro antitumor effect of FA-PEG@ZIF-8@CIP under ultrasound irradiation.

We next investigated intracellular ROS generation using the ROS-sensitive fluorescent probe DCFH-DA. As shown in Figure 2E, all ultrasound-treated groups exhibited stronger green fluorescence than their corresponding non-ultrasound groups, confirming that ultrasound irradiation enhanced ROS production by the sonosensitizing components, including CIP and ZIF-8. Quantitative analysis of ROS fluorescence intensity was performed using ImageJ and is shown in Figure 2F. Among all treatment groups, the FA-PEG@ZIF-8@CIP + US group exhibited the highest ROS signal, indicating the strongest oxidative stress response. This may be attributed to the improved tumor cell targeting conferred by FA-PEG, which promoted greater nanoparticle accumulation and thereby enhanced ROS generation under ultrasound irradiation.

To further determine whether FA-PEG@ZIF-8@CIP induced immunogenic cell death (ICD), we examined the expression of high-mobility group box 1 (HMGB1), calreticulin (CRT), and extracellular ATP release in treated tumor cells. As shown in Figure 2G, the FA-PEG@ZIF-8@CIP + US group displayed decreased nuclear HMGB1 fluorescence

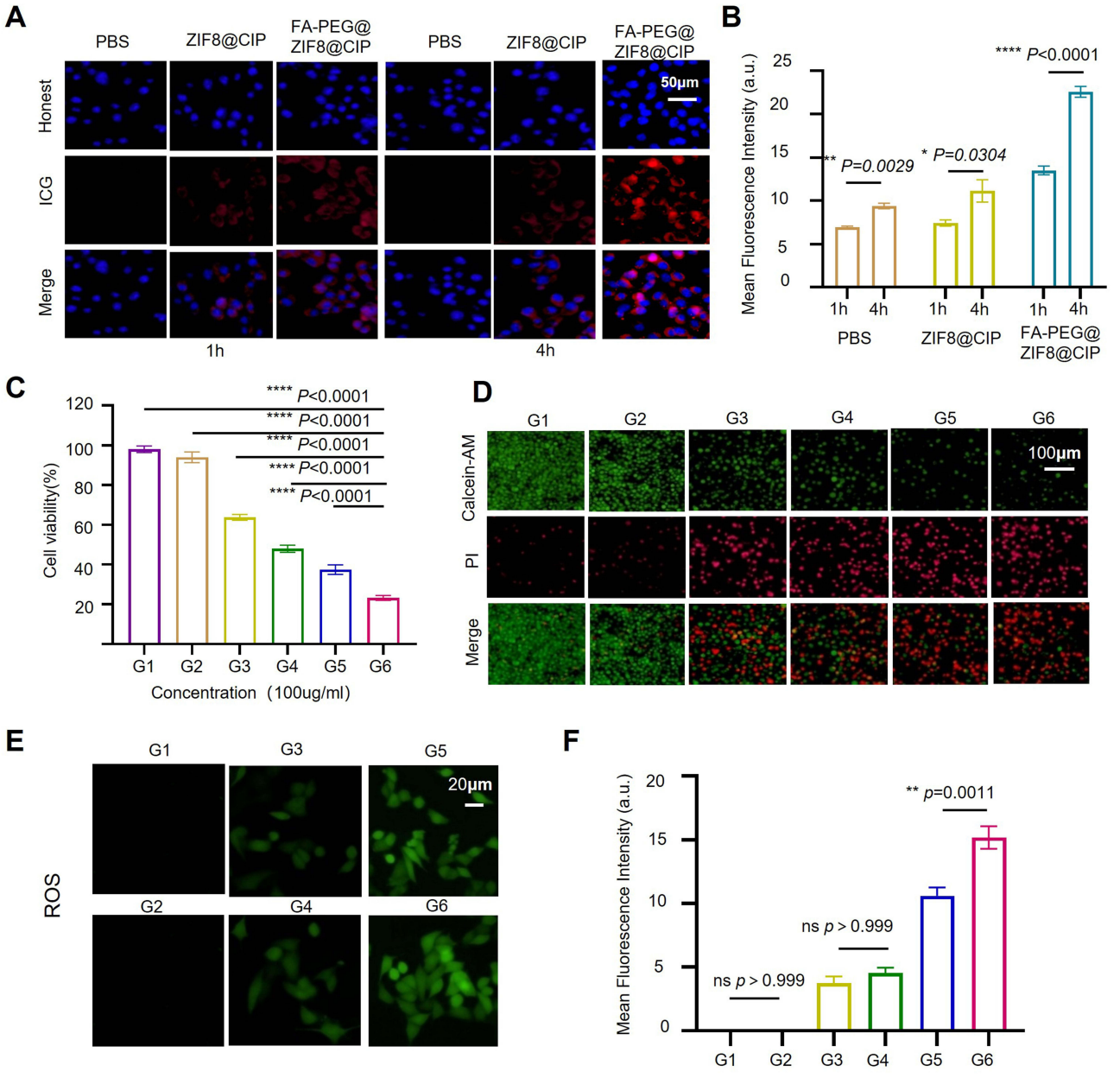

Figure 2 Continued.

https://doi.org/10.2147/IJN.S589815

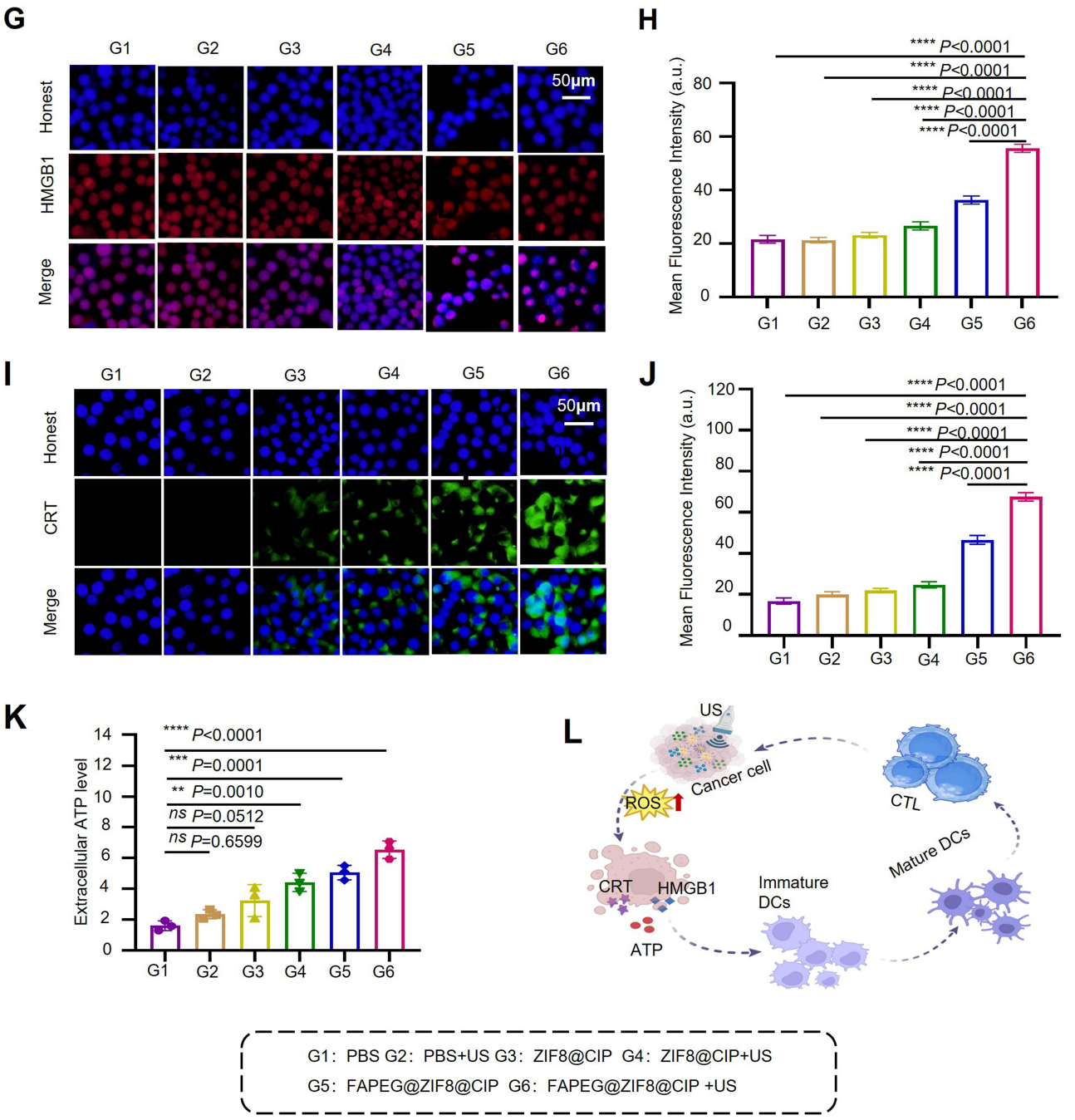

Figure 2 In vitro cellular uptake, cytotoxicity, ROS generation, and ICD induction by FA-PEG@ZIF-8@CIP. (**A**) Fluorescence images of 4T1 cells after incubation with PBS, ZIF-8@CIP, or FA-PEG@ZIF-8@CIP for 1 h or 4 h. Scale bar: 50 μm. (**B**) Quantitative analysis of mean fluorescence intensity in 4T1 cells treated with PBS, ZIF-8@CIP, or FA-PEG@ZIF-8@CIP for 1 h or 4 h (n = 3, mean ± SD). (**C**) Cell viability of different treatment groups at the same concentration (n = 3, mean ± SD). (**D**) Live/dead staining images of 4T1 cells after different treatments. Scale bar: 100 μm. (**E**) Fluorescence images showing intracellular ROS generation under different treatment conditions. Scale bar: 20 μm. (**F**) Quantitative analysis of ROS fluorescence intensity in each group (n = 3, mean ± SD). (**G**) Representative fluorescence images showing HMGB1 expression (red) in cells after different treatments. Scale bar: 50 μm. (**H**) Quantitative analysis of HMGB1 fluorescence intensity in each group (n = 3, mean ± SD).(**I**) Representative fluorescence images showing CRT expression (green) in cells after different treatments. Scale bar: 50 μm. (**J**) Quantitative analysis of CRT fluorescence intensity in each group (n = 3, mean ± SD). (**K**) Extracellular ATP levels after different treatments (n = 3, mean ± SD). (**L**) Schematic illustration of the mechanism by which FA-PEG@ZIF-8@CIP-induced ICD promotes dendritic cell maturation. The figure was created using BioRender. The red arrows indicate increased ROS levels. Ultrasound parameters: 1.0 MHz, 1.5 W/cm^2, 50% duty cycle, 1 min. *p < 0.05, **p < 0.01, ***p < 0.001, ****p < 0.0001.

Abbreviation: ns, not significant.

together with enhanced extranuclear fluorescence, indicating HMGB1 translocation. In contrast, HMGB1 fluorescence in the PBS group remained mainly confined to the nucleus. Quantitative analysis in Figure 2H further showed that the fluorescence intensity in the FA-PEG@ZIF-8@CIP + US group was significantly higher than that in the other groups. Similarly, CRT fluorescence images (Figure 2I) and mean fluorescence intensity analysis (Figure 2J) showed that the FA-PEG@ZIF-8@CIP + US group exhibited the strongest CRT exposure among all groups. In addition, extracellular ATP levels were markedly increased in this group (Figure 2K), further supporting the occurrence of ICD. Collectively, these results demonstrate that FA-PEG@ZIF-8@CIP, upon ultrasound irradiation, effectively induces ICD in 4T1 cells. As illustrated in Figure 2L, the core cytotoxic mechanism of sonodynamic therapy is closely associated with ROS generation and subsequent ICD induction.

Analysis of Nanoparticle Contrast Imaging in Vitro and in Vivo

In Vitro Contrast Imaging Performance

To evaluate the in vitro ultrasound imaging performance of the nanoparticles, suspensions of FA-PEG@ZIF-8@CIP, ZIF-8@CIP and ZIF-8 at defined concentrations were prepared, with PBS and SonoVue (SV) serving as controls. As shown in Figure 3A and B, under contrast-enhanced ultrasound mode, the PBS group showed almost no change in signal intensity as the mechanical index (MI) increased, indicating the absence of contrast-enhancing capability. In contrast, the SV group exhibited a gradual increase in signal intensity when the MI increased from 0.1 to 0.3, followed by a decline at higher MI values, suggesting limited stability under these conditions.

By comparison, both the FA-PEG@ZIF-8@CIP, ZIF-8@CIP and ZIF-8 groups showed progressively enhanced ultrasound signals with increasing MI. Notably, the imaging performance of the ZIF-8 and FA-PEG@ZIF-8@CIP groups was comparable, which is likely attributable to their similar ZIF-8 content. These findings indicate that the ultrasound contrast effect mainly originated from the ZIF-8 component. This behavior may be associated with the porous structure, high specific surface area, and favorable gas adsorption capacity of ZIF-8, which could reduce the cavitation threshold and facilitate acoustic cavitation under ultrasound irradiation.[42,43] As a result, stronger acoustic scattering was generated, leading to increased signal intensity in the contrast-enhanced ultrasound images.

In Vivo Contrast Imaging Performance

Given the favorable in vitro imaging performance, we next evaluated the in vivo contrast-enhanced ultrasound imaging capability of the nanoparticles in 4T1 tumor-bearing mice. As shown in Figure 3C, the tumor regions are outlined by green dotted circles. Before injection, no obvious contrast-enhanced signal was observed in the tumor area. After intravenous administration of the formulations, enhanced signals became detectable within the tumor region under contrast-enhanced ultrasound mode. Moreover, the signal intensity gradually increased with increasing MI.

Compared with the PBS and SV groups, both the FA-PEG@ZIF-8@CIP, ZIF-8@CIP and ZIF-8 groups exhibited stronger contrast signals in the tumor region. Quantitative analysis (Figure 3D) further confirmed that the ultrasound contrast intensity increased progressively with MI. Importantly, the FA-PEG@ZIF-8@CIP group showed slightly stronger contrast enhancement than the ZIF-8 group in vivo. This difference may be attributed to FA-PEG-mediated active targeting, which promoted greater nanoparticle accumulation within the tumor tissue and thereby enhanced the local imaging effect. Collectively, these results demonstrate that FA-PEG@ZIF-8@CIP possesses effective contrast-enhanced ultrasound imaging capability both in vitro and in vivo, supporting its potential application in imaging-guided tumor theranostics.

Analysis of the in Vivo Antitumor Efficacy of FA-PEG@ZIF8@CIP

Encouraged by the pronounced in vitro antitumor activity of FA-PEG@ZIF8@CIP, we next investigated its biodistribution and therapeutic performance in vivo. Prior to systemic administration, a hemolysis assay confirmed the favorable hemocompatibility of FA-PEG@ZIF8@CIP, indicating its suitability for intravenous delivery (Figure S4).

To assess in vivo antitumor efficacy, 4T1 tumor-bearing mice were randomly assigned to six groups: PBS, PBS+US, ZIF8@CIP, ZIF8@CIP+US, FA-PEG@ZIF8@CIP, and FA-PEG@ZIF8@CIP+US. Treatments were administered every other day, followed by ultrasound irradiation (1.0 MHz, 2.5 W cm^{-2}, 50% duty cycle, 5 min) at 6 h post-injection

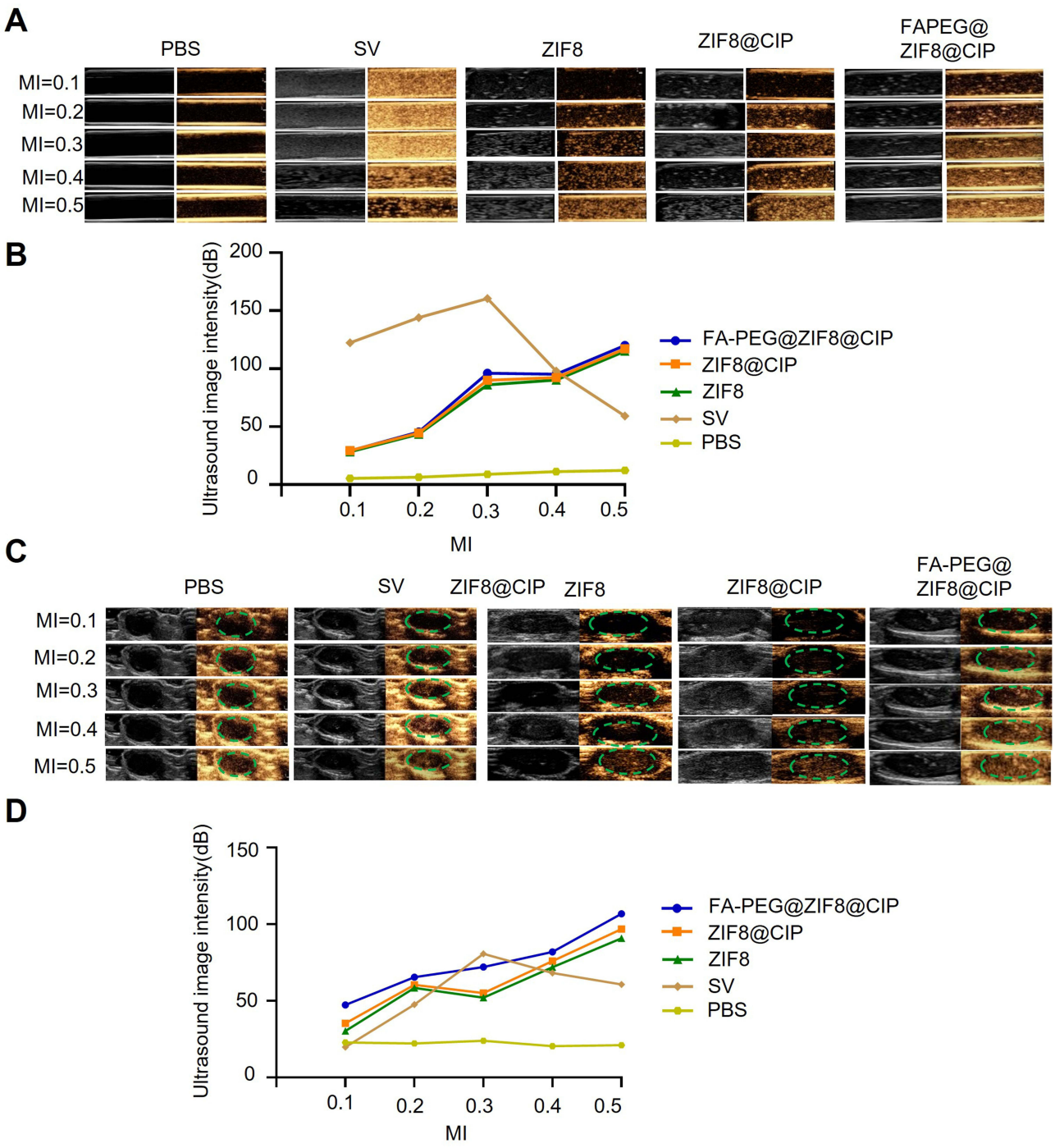

Figure 3 In vitro and in vivo contrast-enhanced ultrasound imaging of different agents. (**A**) In vitro contrast-enhanced ultrasound images of different agents under different mechanical index (MI) settings. (**B**) Quantitative analysis of in vitro ultrasound contrast intensity for different agents. (**C**) In vivo contrast-enhanced ultrasound images of different agents. The green dotted circles indicate the tumor regions. (**D**) Quantitative analysis of in vivo ultrasound contrast intensity for different agents.

(Figure 4A). To further examine in vivo distribution, mice were intravenously injected with free ICG or FA-PEG @ZIF8@CIP/ICG, and fluorescence imaging was performed at different time points. As shown in Figure 4B, fluorescence signals were detectable at the tumor site as early as 1 h after administration of FA-PEG@ZIF8@CIP/ICG. Notably, fluorescence remained clearly visible in the tumor region at 24 h, whereas the signal in the free ICG group declined markedly. At 48 h post-injection, ex vivo imaging of tumors and major organs revealed substantially stronger fluorescence accumulation in tumors from the FA-PEG@ZIF8@CIP group than in the control group (Figure 4C). Consistently,

 https://doi.org/10.2147/IJN.S589815

quantitative analysis of ex vivo fluorescence intensity further confirmed that the tumor fluorescence signal was highest in the FA-PEG@ZIF8@CIP group (Figure 4D). These findings indicate that FA-PEG functionalization improves tumor accumulation and retention of the nanoplatform in vivo.

No significant body weight loss was observed in any group during the treatment period, suggesting acceptable systemic tolerance (Figure 4E). At the experimental endpoint, the FA-PEG@ZIF8@CIP+US group exhibited the lowest mean tumor weight among all groups, indicating the strongest tumor suppression efficacy (Figure 4F). Consistently, mean tumor growth curves (Figure 4G) and individual tumor growth profiles (Figure 4H) both showed that FA-PEG @ZIF8@CIP+US treatment most effectively inhibited tumor progression throughout the observation period. Representative photographs of excised tumors further supported this result, with the smallest tumor size observed in the FA-PEG@ZIF8@CIP+US group (Figure 4I). To eliminate interference from other factors, the treatment duration, drug dosage (100 μg/mL) throughout the study, and treatment frequency were kept consistent across all mouse groups. In addition, ultrasound monitoring demonstrated an obvious reduction in tumor volume after treatment in the FA-PEG @ZIF8@CIP+US group (Figure 4J), further supporting its robust therapeutic efficacy in vivo.

Histological analyses provided further evidence of the enhanced antitumor effect. H&E staining revealed more extensive tumor cell destruction in the FA-PEG@ZIF8@CIP+US group than in the other groups (Figure 4K). Ki67 staining showed the lowest proliferative activity in this group (Figure 4L), while TUNEL staining displayed the strongest apoptotic signal, indicating the highest level of tumor cell apoptosis (Figure 4M). Importantly, no obvious pathological abnormalities were observed in major organs by H&E staining at the endpoint (Figure S5), and serum biochemical and immunological parameters remained comparable among the groups (Figure S6), supporting the in vivo biosafety of the treatment.

Taken together, these results demonstrate that FA-PEG@ZIF8@CIP combined with ultrasound achieves the most effective tumor suppression in vivo. This enhanced therapeutic performance is likely associated with improved tumor accumulation mediated by FA-PEG modification, together with ultrasound-triggered amplification of therapeutic activity. Therefore, FA-PEG@ZIF8@CIP represents a promising theranostic nanoplatform for safe and effective TNBC treatment.

Evaluation of the in Vivo Antitumor Immune Response Induced by Nanoparticles

To investigate the in vivo immune response triggered by FA-PEG@ZIF8@CIP, immune cell populations in lymph nodes, tumors, and spleens were analyzed by flow cytometry. Because effective T-cell priming depends on antigen presentation by dendritic cells (DCs), we first quantified DC maturation in tumor-draining lymph nodes. As shown in Figure 5A, the FA-PEG@ZIF8@CIP+US group markedly increased the proportion of mature DCs to 28.6%, corresponding to a 2.7-fold increase relative to the PBS group. This result indicates that the combined treatment effectively promoted antigen-presenting cell activation in vivo.

We next examined immune cell infiltration within the tumor microenvironment. Compared with the PBS group, the proportions of tumor-infiltrating $CD8^+$ T cells and $CD4^+$ T cells in the FA-PEG@ZIF8@CIP+US group increased by 2.9-fold and 2.6-fold, respectively (Figure 5B and C), indicating enhanced recruitment of effector T cells into tumor tissue. Consistently, immunofluorescence staining further confirmed increased infiltration of $CD8^+$ T cells (green) and $CD4^+$ T cells (red) in tumors following FA-PEG@ZIF8@CIP+US treatment (Figure S7).

In addition to increased T-cell infiltration, the cytotoxic activity of intratumoral T cells was also enhanced. As shown in Figure 5D, the proportion of Granzyme B^+ $CD8^+$ T cells, a marker of cytotoxic effector function, was elevated by 2.8-fold in the FA-PEG@ZIF8@CIP+US group compared with the PBS group. In parallel, the proportion of immunosuppressive regulatory T cells (Tregs) was significantly reduced (Figure 5E), suggesting partial reversal of the immunosuppressive tumor microenvironment.

A similar trend was observed in the spleen, where the proportions of $CD8^+$ and $CD4^+$ T cells (Figure S8) or $CD3^+$ and $CD4^+$ T cells (Figure S9) were also increased after FA-PEG@ZIF8@CIP+US treatment. Moreover, the percentage of IFN-γ^+CD8^+ T cells increased by 4.8-fold relative to the control group (Figure 5F), further supporting enhanced systemic activation of antitumor cytotoxic T-cell responses.

Taken together, these results demonstrate that FA-PEG@ZIF8@CIP, when combined with ultrasound, not only suppresses primary tumor growth but also elicits a robust antitumor immune response. This immune activation is

 https://doi.org/10.2147/IJN.S589815

characterized by enhanced DC maturation, increased infiltration of effector T cells, elevated cytotoxic function, and reduced immunosuppressive Treg accumulation, collectively supporting the immunomodulatory potential of this nanoplatform in vivo.

Analysis of the Therapeutic Efficacy in a Nanoparticle Lung Metastasis Model in Vivo

Encouraged by the pronounced antitumor efficacy of FA-PEG@ZIF8@CIP, we further evaluated its antimetastatic activity in a 4T1 lung metastasis model (Figure 6A). As shown in Figure 6B, numerous metastatic nodules were

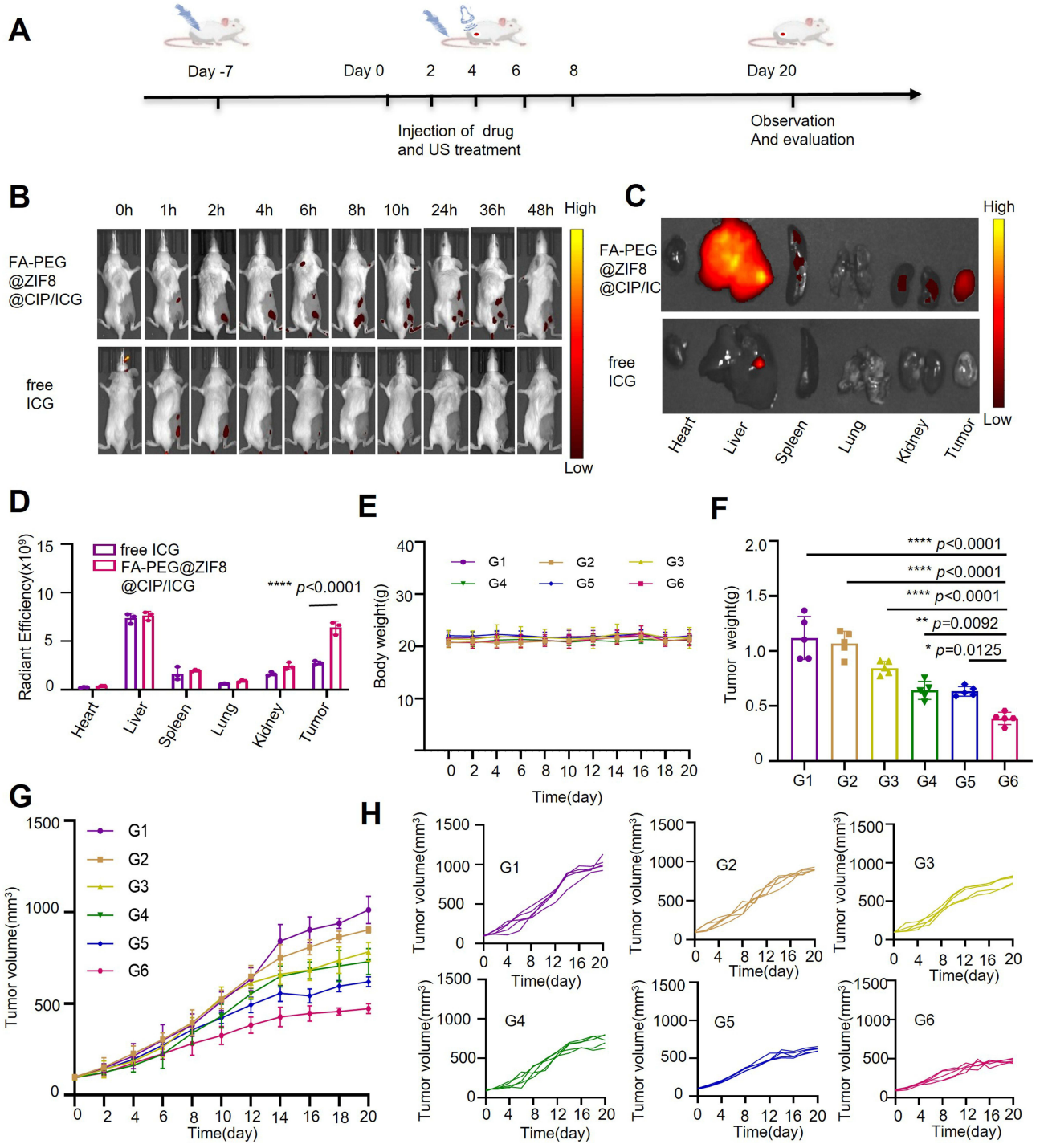

Figure 4 Continued.

https://doi.org/10.2147/IJN.S589815

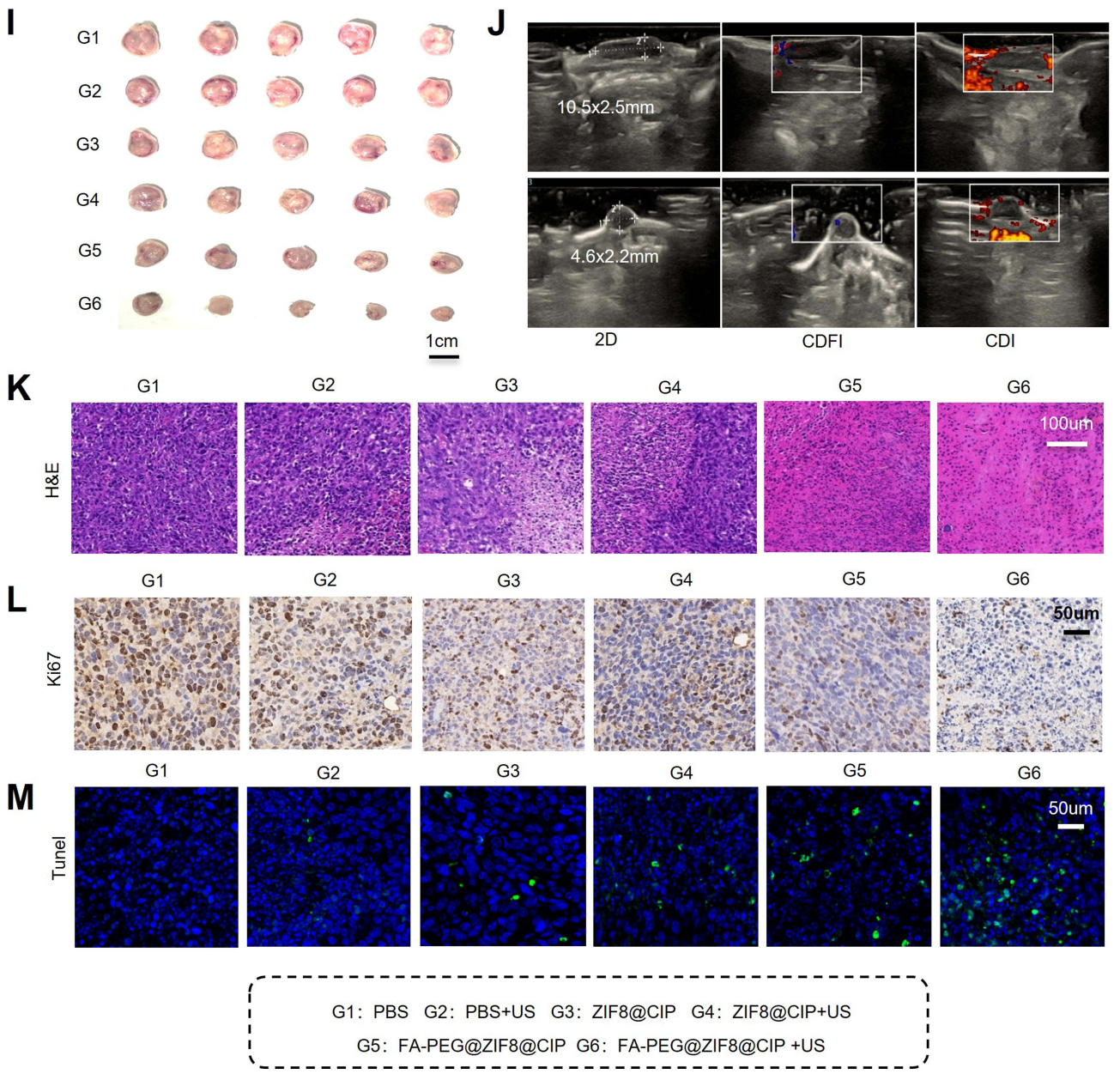

Figure 4 In vivo biodistribution and antitumor efficacy of FA-PEG@ZIF-8@CIP in 4T1 tumor-bearing mice. (**A**) Schematic illustration of the establishment of the 4T1 tumor-bearing mouse model and the treatment regimen. (**B**) In vivo fluorescence imaging showing the biodistribution of FA-PEG@ZIF-8@CIP and free ICG at different time points (ICG: 3.5 mg/kg). (**C**) Ex vivo fluorescence images of dissected tumors and major organs collected at the experimental endpoint. (**D**) Quantitative analysis of ex vivo fluorescence intensity in tumors and major organs. (**E**) Changes in mean body weight of mice in each group during treatment (n = 5, mean ± SD). (**F**) Mean tumor weight of each group at the experimental endpoint (n = 5, mean ± SD). (**G**) Mean tumor growth curves of 4T1 tumor-bearing mice in each group (n = 5, mean ± SD). (**H**) Individual tumor growth curves of mice in all treatment groups. (**I**) Representative photographs of excised tumors from each group at the endpoint (n = 5). Scale bar: 1 cm. (**J**) Representative ultrasound images of tumors before and after treatment. (**K–M**) Representative images of tumor sections stained with H&E (scale bar: 100 μm), Ki67 (scale bar: 50 μm), and TUNEL (scale bar: 50 μm), respectively, from each group.Ultrasound parameters: 1.0 MHz, 1.5 W/cm^2, 50% duty cycle, 5 min. *p < 0.05, **p < 0.01, ****p < 0.0001.

Abbreviation: ns, not significant.

observed in the PBS, ZIF8@CIP and FA-PEG@ZIF8@CIP groups, whereas only a few metastatic lesions were detected in the FA-PEG@ZIF8@CIP+US group. Quantitative analysis further confirmed that FA-PEG@ZIF8@CIP+US significantly reduced the number of pulmonary metastatic nodules compared with the control groups (Figure 6C). Consistently, the lung weight in the FA-PEG@ZIF8@CIP+US group was also lower than that in the other groups (Figure 6D), which is likely associated with the markedly reduced metastatic burden.

https://doi.org/10.2147/IJN.S589815

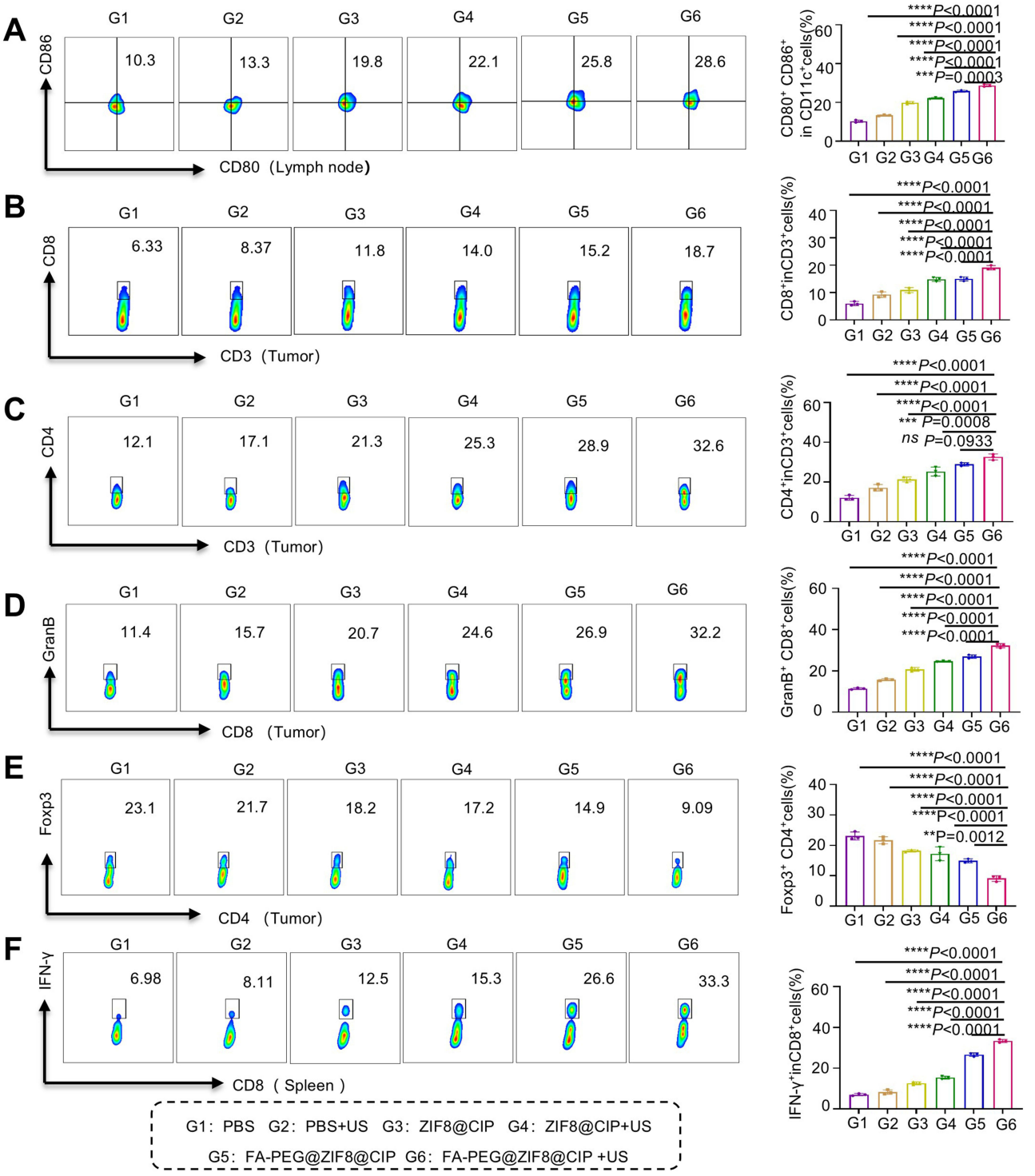

Figure 5 In vivo immune activation induced by FA-PEG@ZIF-8@CIP treatment. (**A**) Flow cytometry analysis and quantification of mature dendritic cells (DCs, $CD11c^+CD80^+CD86^+$) in lymph nodes (n = 3, mean ± SD). **B-E**) Flow cytometry analysis and quantification of $CD3^+CD8^+$ T cells, $CD3^+CD4^+$ T cells, $CD8^+$Granzyme B^+ T cells, and $CD4^+Foxp3^+$ T cells in tumor tissues (n = 3, mean ± SD). (**F**) Flow cytometry analysis and quantification of $CD8^+IFN\text{-}\gamma^+$ T cells in spleens (n = 3, mean ± SD). Ultrasound parameters: 1.0 MHz, 1.5 W/cm^2, 50% duty cycle, 5 min. **p < 0.01, ***p < 0.001, ****p < 0.0001.
Abbreviation: ns, not significant.

Histological examination of lung tissues provided further evidence for the antimetastatic effect. As shown in Figure 6E, lung sections from the PBS group displayed extensive metastatic infiltration, with multiple well-defined tumor lesions distributed throughout the pulmonary parenchyma. Higher-magnification images revealed dense tumor cell

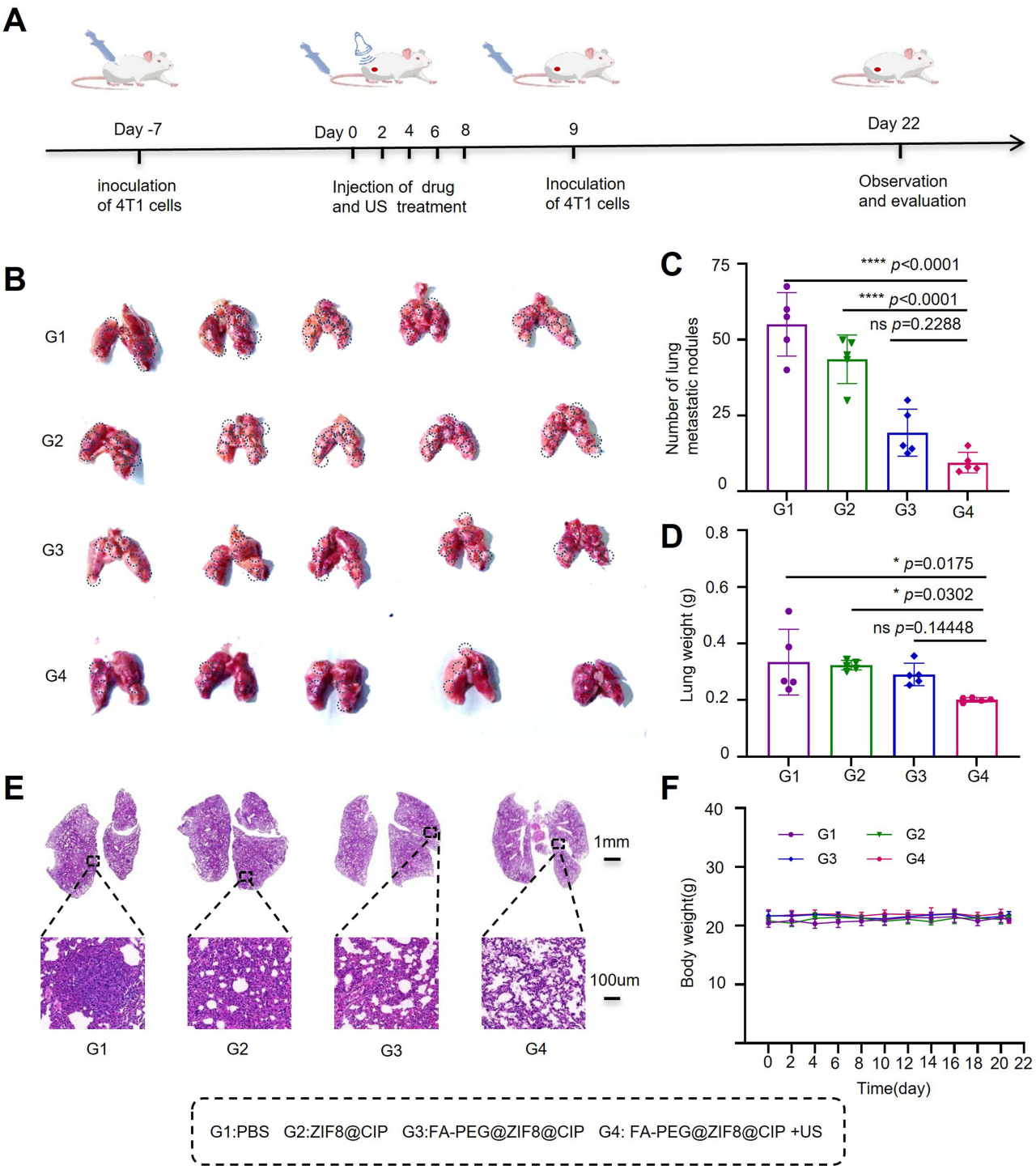

Figure 6 Therapeutic effect of FA-PEG@ZIF-8@CIP in the lung metastasis model. (**A**) Schematic illustration of the establishment of the lung metastasis model and the treatment regimen. (**B**) Representative photographs of lungs harvested from each group at the experimental endpoint (n = 5). Black dotted circles indicate metastatic tumor nodules in the lungs. (**C**) Number of lung metastatic nodules in each group at the experimental endpoint (n = 5, mean ± SD). (**D**) Lung weight of each group at the experimental endpoint (n = 5, mean ± SD). (**E**) Representative H&E-stained lung sections from each group at the endpoint. The black dashed squares indicate the regions of interest, and the black dashed lines indicate the magnified areas. (**F**) Mean body weight of mice in each group at the experimental endpoint (n = 5, mean ± SD). *p < 0.05, ****p < 0.0001.
Abbreviation: ns, not significant.

clusters that largely disrupted the normal alveolar architecture and compressed the surrounding lung tissue. In contrast, lung tissues from the FA-PEG@ZIF8@CIP+US group largely retained intact alveolar structures with a typical honeycomb-like morphology, and metastatic lesions were markedly reduced. These histopathological findings are consistent with the gross observations and quantitative analyses described above.

https://doi.org/10.2147/IJN.S589815

Importantly, no significant body weight loss was observed in any treatment group during the experimental period (Figure 6F), indicating acceptable systemic tolerance of the treatment. Taken together, these results demonstrate that FA-PEG@ZIF8@CIP, when combined with ultrasound irradiation, effectively suppresses lung metastasis in vivo while maintaining a favorable safety profile.

Conclusion

We developed an FA-PEG-functionalized, ciprofloxacin-loaded ZIF-8 nanoplatform (FA-PEG@ZIF-8@CIP) as a theranostic strategy for triple-negative breast cancer (TNBC). ZIF-8 served not only as a drug carrier but also exhibited intrinsic sonosensitizer properties. Its degradation releases Zn^{2+}, which induces tumor cell apoptosis and enhances reactive oxygen species generation under ultrasound irradiation. Ciprofloxacin, repurposed as an anticancer agent, directly inhibits tumor cells and synergistically enhances sonodynamic therapy through Zn^{2+} chelation. FA-PEG modification improved tumor-targeting efficiency via folate receptor-mediated uptake and enabled pH-responsive drug release in the acidic tumor microenvironment. This system also integrates ultrasound imaging for early tumor detection, enhancing its diagnostic and therapeutic capabilities. In vivo, the FA-PEG@ZIF-8@CIP + US group exhibited a tumor inhibition rate of 75.75%, 4.21-fold higher than the PBS group. Additionally, this treatment enhanced antitumor immunity, as indicated by increased $GranB^{+}$ expression (32.2%) and reduced Treg cell infiltration (9.09%) in tumor tissues. Overall, our findings demonstrate that this nanoplatform induces immunogenic cell death and activates robust antitumor immunity, offering a multi-mechanistic synergy combining sonodynamic therapy, chemotherapy, and immunomodulation. This strategy significantly enhances TNBC treatment efficacy and shows strong potential for clinical translation.

Acknowledgments

The authors thank for the technical support of the Modern Analysis and Computer Center of Zhengzhou University.

Funding

This work was supported by the National Natural Science Foundation of Henan province (grant number 252300421151), the National Natural Science Foundation of China (grant number 82371987), the Key Research and Development Project in Henan Province (grant number 221111310400), the Henan Rehabilitation Clinical Medical Research Center and Medical Appropriate Technology Promotion Project of Henan Province (grant number SYJS2022018), the Henan Provincial Science and Technology Research Project (grant number 242102311104), the Henan Provincial Science and Technology Research Project (grant number 232102311063).

Disclosure

The authors declare no competing interests in this work.

References

1. Zidan J. Androgen receptor expression in female patients with triple-negative breast cancer: relation to clinical, pathological, and ethnical data and comparison with non–triple-negative breast cancer. *J Clin Oncol*. 2023;41(16_suppl):e13022. doi:10.1200/jco.2023.41.16_suppl.e13022
2. López-Tejada A, Blaya-Cánovas JL, Cara FE, et al. Signature-based repurposed drugs resemble the inhibition of TGFβ-induced NDRG1 as potential therapeutics for triple-negative breast cancer. *Int J Biol Sci*. 2025;21(9):3949–3967. doi:10.7150/ijbs.112645
3. Rodriguez Gonzalez G, Tuset Der-abrain N, Prieto Garcia A, et al. De-escalation neoadjuvant chemotherapy in triple negative breast cancer. *J Clin Oncol*. 2024;42(16_suppl):e12520. doi:10.1200/jco.2024.42.16_suppl.e12520
4. Ghosh S, Javia A, Shetty S, et al. Triple negative breast cancer and non-small cell lung cancer: clinical challenges and nano-formulation approaches. *J Controlled Release*. 2021;337:27–58. doi:10.1016/j.jconrel.2021.07.014
5. Xing X, Zhao S, Xu T, et al. Advances and perspectives in organic sonosensitizers for sonodynamic therapy. *Coordin Chem Rev*. 2021;445 (214087):214087. doi:10.1016/j.ccr.2021.214087
6. Son S, Kim JH, Wang X, et al. Multifunctional sonosensitizers in sonodynamic cancer therapy. *Chem Soci Rev*. 2020;49(11):3244–3261. doi:10.1039/c9cs00648f
7. Wang W, Pan X, Yang H, et al. Bioactive metal–organic frameworks with specific metal–nitrogen (M–N) active sites for efficient sonodynamic tumor therapy. *ACS NANO*. 2021;15(12):20003–20012. doi:10.1021/acsnano.1c07547
8. Collins VG, Hutton D, Hossain-Ibrahim K, et al. The abscopal effects of sonodynamic therapy in cancer. *Br J Cancer*. 2024;132(5):409–420. doi:10.1038/s41416-024-02898-y

9. Yu J, Hu J-R, Tian Y, et al. Nanosensitizer-assisted sonodynamic therapy for breast cancer. *J Nanobiotechnol*. 2025;23(1):281. doi:10.1186/s12951-025-03311-3
10. Pan X, Wang H, Wang S, et al. Sonodynamic therapy (SDT): a novel strategy for cancer nanotheranostics. *SciChina Life Sci*. 2018;61(4):415–426. doi:10.1007/s11427-017-9262-x
11. Wang X, Zhong X, Gong F, et al. Newly developed strategies for improving sonodynamic therapy. *Mater Horiz*. 2020;7(8):2028–2046. doi:10.1039/d0mh00613k
12. Xu Q, Zhang M, Huang Q, et al. Organic AIE nanoradiosensitizer potentiates X-Ray triggered continuous reactive oxygen species generation for potent cancer radioimmunotherapy. *Adv Mater*. 2025;37(35):e2502898. doi:10.1002/adma.202502898
13. Yang Y, Wang N, Yan F, et al. Metal-organic frameworks as candidates for tumor sonodynamic therapy: designable structures for targeted multifunctional transformation. *Acta Biomater*. 2024;181:67–97. doi:10.1016/j.actbio.2024.04.037
14. Wang D, Wu Q, Ren X, et al. Tunable zeolitic imidazolate framework-8 nanoparticles for biomedical applications. *Small Methods*. 2023;8(3):e2301270. doi:10.1002/smtd.202301270
15. Vodyashkin AA, Sergorodceva AV, Kezimana P, et al. Metal-organic framework (MOF)-A universal material for biomedicine. *Int J Mol Sci*. 2023;24(9):7819. doi:10.3390/ijms24097819
16. Shi Y, Zeng M, Casals E, et al. Metal and covalent organic frameworks meet OB-GYN: advancing applications in women's health and pregnancy care. *Small*. 2025;21(33):e2504366. doi:10.1002/smll.202504366
17. Rostami J, Benselfelt T, Maddalena L, et al. Shaping 90 wt% NanoMOFs into robust multifunctional aerogels using tailored bio-based nanofibrils. *Adv Mater*. 2022;34(38):e2204800. doi:10.1002/adma.202204800
18. Siboro PY, Nguyen VKT, Miao Y-B, et al. Ultrasound-activated, tumor-specific in situ synthesis of a chemotherapeutic agent using ZIF-8 nanoreactors for precision cancer therapy. *ACS NANO*. 2022;16(8):12403–12414. doi:10.1021/acsnano.2c03587
19. Sun Y, Zheng L, Yang Y, et al. Metal–organic framework nanocarriers for drug delivery in biomedical applications. *Nano-Micro Letters*. 2020;12(1):103. doi:10.1007/s40820-020-00423-3
20. Zhuang J, Young AP, Tsung C-K. Integration of biomolecules with metal–organic frameworks. *SMALL*. 2017;13(32). doi:10.1002/smll.201700880
21. Liu Z, Gao Y, Shao W, et al. Multidimensional applications and challenges of metal–organic frameworks (MOFs) in biomedicine: from drug safety evaluation to drug delivery. *J Biomed Mater Res A*. 2025;113(7):e37952. doi:10.1002/jbm.a.37952
22. Pan X, Bai L, Wang H, et al. Metal–organic-framework-derived carbon nanostructure augmented sonodynamic cancer therapy. *Advanced Materials*. 2018;30(23):e1800180. doi:10.1002/adma.201800180
23. Lai -C-C, Chen C-Y, Chang T-H. Predicting pathological complete response following neoadjuvant therapy in patients with breast cancer: development of machine learning–based prediction models in a retrospective study. *JMIR Cancer*. 2025;11:e64685. doi:10.2196/64685
24. Liu W, Yan Q, Xia C, et al. Correction: recent advances in cell membrane coated metal–organic frameworks (MOFs) for tumor therapy. *J Mater Chem B*. 2021;9(21):4411. doi:10.1039/d1tb90082j
25. Sharma P, Goyal R, Sharma A, et al. Insights on fluoroquinolones in cancer therapy: chemistry and recent developments. *Mater Today Chem*. 2020;17(100296). doi:10.1016/j.mtchem.2020.100296
26. Huang C-Y, Yang J-L, Chen -J-J, et al. Fluoroquinolones suppress TGF-β and PMA-induced MMP-9 production in cancer cells: implications in repurposing quinolone antibiotics for cancer treatment. *Int J Mol Sci*. 2021;22(21):11602. doi:10.3390/ijms222111602
27. Chen JS, Chi CW, Lai CT, et al. Ciprofloxacin exerts anti-tumor effects in vivo through cGAS-STING activation and modulates tumor microenvironment. *Cells*. 2025;14(13):1010. doi:10.3390/cells14131010
28. Beberok A, Wrześniok D, Rok J, et al. Ciprofloxacin triggers the apoptosis of human triple-negative breast cancer MDA-MB-231 cells via the p53/Bax/Bcl-2 signaling pathway. *Int J Oncol*. 2018;52(5):1727–1737. doi:10.3892/ijo.2018.4310
29. Ramos VC, Reyes CBG, García GM, et al. ZIF-8 and its magnetic functionalization as vehicle for the transport and release of ciprofloxacin. *Pharmaceutics*. 2022;14(11):2546. doi:10.3390/pharmaceutics14112546
30. Chu Z, Chen H, Wang P, et al. Phototherapy using a fluoroquinolone antibiotic drug to suppress tumor migration and proliferation and to enhance apoptosis. *ACS NANO*. 2022;16(3):4917–4929. doi:10.1021/acsnano.2c00854
31. Ding L, Liang X, Ma J, et al. Sono-triggered biomimetically nanoantibiotics mediate precise sequential therapy of MRSA-induced lung infection. *Adv Mater*. 2024;36(46):e2403612. doi:10.1002/adma.202403612
32. Ding B, Chen H, Tan J, et al. ZIF-8 nanoparticles evoke pyroptosis for high-efficiency cancer immunotherapy. *Angewandte Chemie Int*. 2023;62(10):e202215307. doi:10.1002/anie.202215307
33. Zeng X, Wang X, Zhao Y, et al. Dual-mode immunotherapy: ultrasound responsive zinc-based nano-contract agents synergistically activate the GAS-STING pathway for enhanced tumor sono-metalloimmunotherapy. *Ultrason Sonochem*. 2025;120(107494):107494. doi:10.1016/j.ultsonch.2025.107494
34. Narmani A, Rezvani M, Farhood B, et al. Folic acid functionalized nanoparticles as pharmaceutical carriers in drug delivery systems. *Drug Develop Res*. 2019;80(4):404–424. doi:10.1002/ddr.21545
35. Marshalek JP, Sheeran PS, Ingram P, et al. Intracellular delivery and ultrasonic activation of folate receptor-targeted phase-change contrast agents in breast cancer cells in vitro. *J Control Release*. 2016;243:69–77. doi:10.1016/j.jconrel.2016.09.010
36. Chen WT, Kang ST, Lin JL, et al. Targeted tumor theranostics using folate-conjugated and camptothecin-loaded acoustic nanodroplets in a mouse xenograft model. *Biomaterials*. 2015;53:699–708. doi:10.1016/j.biomaterials.2015.02.122
37. Zhong S, Zhang H, Liu Y, et al. Folic acid functionalized reduction-responsive magnetic chitosan nanocapsules for targeted delivery and triggered release of drugs. *Carbohydrate Polymers*. 2017;168:282–289. doi:10.1016/j.carbpol.2017.03.083
38. He J, Ding R, Tao Y, et al. Folic acid-modified reverse micelle-lipid nanocapsules overcome intestinal barriers and improve the oral delivery of peptides. *Drug Delivery*. 2023;30(1):2181744. doi:10.1080/10717544.2023.2181744
39. Ning S, Lyu M, Zhu D, et al. Type-I AIE photosensitizer loaded biomimetic system boosting cuproptosis to inhibit breast cancer metastasis and rechallenge. *ACS Nano*. 2023;17(11):10206–10217. doi:10.1021/acsnano.3c00326
40. Mi X, Hu M, Dong M, et al. Folic acid decorated zeolitic imidazolate framework (ZIF-8) loaded with baicalin as a nano-drug delivery system for breast cancer therapy. *Int J Nanomed*. 2021;16:8337–8352. doi:10.2147/IJN.S340764
41. Wei M, Bai J, Shen X, et al. Glutathione-exhausting nanoprobes for NIR-II fluorescence imaging-guided surgery and boosting radiation therapy efficacy via ferroptosis in breast cancer. *ACS NANO*. 2023;17(12):11345–11361. doi:10.1021/acsnano.3c00350

42. Bi K, Wang B, Zhang Y, et al. Contrast-enhanced ultrasound of the pleural cavity: a method to locate pleural catheters and identify fibrous septa. *Ultrasound Med Biol*. 2021;47(5):1261–1268. doi:10.1016/j.ultrasmedbio.2021.01.011
43. Bürkle F, Doll J, Neide A, et al. New perspectives for investigating muscular perfusion response after dietary supplement intake: an exploratory, randomized, double-blind, placebo-controlled crossover trial in healthy young athletes using contrast-enhanced ultrasound (CEUS). *J Int Soc Sports Nutr*. 2022;19(1):397–416. doi:10.1080/15502783.2022.2097018